Contents lists available at ScienceDirect

Ultrasonics - Sonochemistry

journal homepage: www.elsevier.com

Experimental and numerical investigation of acoustic pressures in different liquids

G.S. Bruno Lebon[a, b, *], Iakovos Tzanakis[a, c], Koulis Pericleous[b], Dmitry Eskin[a, d]

[a] Brunel Centre for Advanced Solidification Technology, Brunel University London, Uxbridge UB8 3PH, UK
[b] Computational Science and Engineering Group, University of Greenwich, 30 Park Row, London SE10 9LS, UK
[c] Faculty of Technology, Design and Environment, Oxford Brookes University, Oxford OX33 1HX, UK
[d] Tomsk State University, Tomsk 634050, Russia

ARTICLE INFO

Keywords:
Acoustic cavitation
Sonoprocessing
Ultrasonic melt treatment
Light alloy melts

ABSTRACT

In an attempt to quantify the instantaneous pressure field in cavitating liquids at large forcing signals, pressures were measured in four different liquids contained in vessels with a frequency mode in resonance with the forcing signal. The pressure field in liquid metal was quantified for the first time, with maximum pressures of the order of 10–15 MPa measured in liquid aluminium. These high pressures are presumed to be responsible for deagglomeration and fragmentation of dendritic intermetallics and other inclusions. Numerical modelling showed that acoustic shielding attenuates pressure far from the sonotrode and it is prominent in the transparent liquids studied but less so in aluminium, suggesting that aluminium behaviour is different. Due to acoustic shielding, the numerical model presented cannot adequately capture the pressure field away from the intense cavitation zone, but gives a good qualitative description of the cavitation activity. The results obtained contribute to understanding the process of ultrasonic melt treatment (UST) of metal alloys, while facilitating further the guidelines formulation and reproducible protocols for controlling UST at industrial levels.

1. Introduction

Ultrasonic melt treatment (UST), and the resulting production of high-quality light alloys, is of great interest to the casting, automotive, and aerospace industries. UST refines the grain structure of the treated metallic materials, thereby improving their physical and mechanical properties [1–3]. The high-intensity ultrasonic waves that are introduced into liquid metal induce acoustic cavitation. Acoustic cavitation is associated with the rapid growth and implosive collapse of bubbles. These collapses generate high-speed liquid jets (300–1000 $m s^{-1}$) and local hydrodynamic pressures of the order of GPa [4]. The beneficial effects of ultrasonic melt processing—accelerated diffusion [5], activation of inclusions [3], improved wetting and particles dispersion [6,7], deagglomeration and fragmentation [8,9], leading to degassing [10], refined solidification microstructure [11], and uniform distribution of constituent phases [12]—are attributed to acoustic cavitation and associated stirring. For a fundamental understanding of these effects, an accurate evaluation of the pressure field and distribution of cavitation bubbles in the liquid is required.

The study of cavitation bubble dynamics in liquid metals is difficult due to the high temperatures involved, opacity of the media, and lack of equipment for measuring cavitation activity accurately. Quantitative experimental studies of the processes occurring during melt processing and validation of numerical models describing the phenomenon became available only recently. X-ray imaging technology—in the form of third generation synchrotron radiation sources—was applied for *in situ* studies of bubble dynamics [13], nucleation [14], and fragmentation [15] in liquid aluminium (Al) alloys. However, the small spatial and large temporal scales that are involved in the process hinder clear visualization of the physical processes and, consequently, a deeper insight into the behaviour of cavitation bubbles. This also imposes restrictions on the validation of numerical models [16].

Along with X-ray imaging, acoustic emission measurements can be used to analyse the dynamic process of cavitation. Recently, the ability of measuring acoustic pressures in melts has opened the door to an in-depth understanding of the governing mechanisms of UST [17]. The cavitation noise spectra carry a multitude of information in their respective sub-harmonic, ultra-harmonic, and broadband components

* Corresponding author at: Brunel Centre for Advanced Solidification Technology, Brunel University London, Uxbridge UB8 3PH, UK.
Email address: blebon@gmail.com (G.S.Bruno Lebon)

https://doi.org/10.1016/j.ultsonch.2017.12.002
Received 2 November 2017; Received in revised form 1 December 2017; Accepted 2 December 2017
Available online xxx
1350-4177/

[18]. These spectra provide substantial information on the cavitation regime and enable the measurement of acoustic pressures [19]. The spatial and temporal resolutions of hydrophones place a hard limit on the accuracy of the evaluation of the pressure field in the liquid under treatment: numerical modelling can fill this gap, by evaluating pressure fields with a larger resolution.

Modelling of acoustic cavitation is challenging: the temporal resolution that is required to solve the coupled flow and cavitation equations makes solving the acoustic cavitation models expensive. These models are generally not accurate at high forcing pressures [20]. The models that are used in the literature stem from the equations of motion for mixtures of liquid and gas bubbles by van Wijngaarden [21]. Caflisch *et al.* later established the mathematical basis and applicability of these equations [22]. Other models solving ultrasound propagation in cavitating liquids follow the same approach [23–26]. More recently, these models have been implemented for UST. Specifically, the authors [25] have developed a numerical model that can reasonably predict the pressure field distribution in liquid aluminium.

The literature also suggests modifications to homogeneous cavitation models for acoustic cavitation [27,28] or resolving the physics of individual bubbles and clouds [16,29,30]. Accurate numerical modelling of the physical phenomena occurring during cavitation in a large length-scale multi-phase system is, however, still elusive. Linearization of the van Wijngaarden equation yields good results at low bubble volume fractions (<2%), but only when the effect of bubble resonance is negligible [31]. This is not representative of the regime at which ultrasonic treatment operates, where bubble resonance is expected to play a crucial role. The acoustic shielding effects due to the dynamic changes in the acoustic properties of the cavitation zone cannot be currently quantified at large length and time scales through modelling.

Previously, the effects of various factors (operating temperature, transducer power, and distance from ultrasonic source) were successfully studied [32]. The cavitation profiles in different liquids were characterized and the likely behaviour of liquid aluminium under sonication was inferred by dimensional analysis [18]. Water was deemed a suitable transparent analogue for studying acoustic cavitation in aluminium. In this paper, acoustic pressures are measured in the same four liquids under ultrasonic treatment: water, ethanol, glycerol, and aluminium. The liquids are, however, treated in vessels with a resonance mode corresponding to the driving frequency. In addition the same ultrasonic setup with the same sonotrode is used for all liquids, including molten aluminium. The experimental measurements of pressure are then compared with predictions from the Caflisch equations. The aim of this investigation is to quantify the pressure field in cavitating liquids at large forcing signals, facilitating further the guidelines formulation and reproducible protocols for controlling UST at industrial levels.

2. Setup

2.1. Experimental

A piezoelectric transducer (UIP1000hd) with an operating frequency of 19.6–19.7 kHz introduced ultrasound in a rectangular domain (Fig. 1(a)) via a high performance ceramic sonotrode (SiAlON) with a diameter of 48 mm and length 460 mm. The radiating surface of the vertically mounted sonotrode was immersed 20 mm below the liquid free surface along the tank axis. Three operating acoustic powers, corresponding to the peak-to-peak amplitudes in Table 1, were used. For safety reasons, transducer powers above 70% were avoided as cavitation intensity becomes very severe in this regime. A wattmeter (integrated with the transducer and generator) monitored the acoustic power introduced into the liquid. The acoustic power introduced into

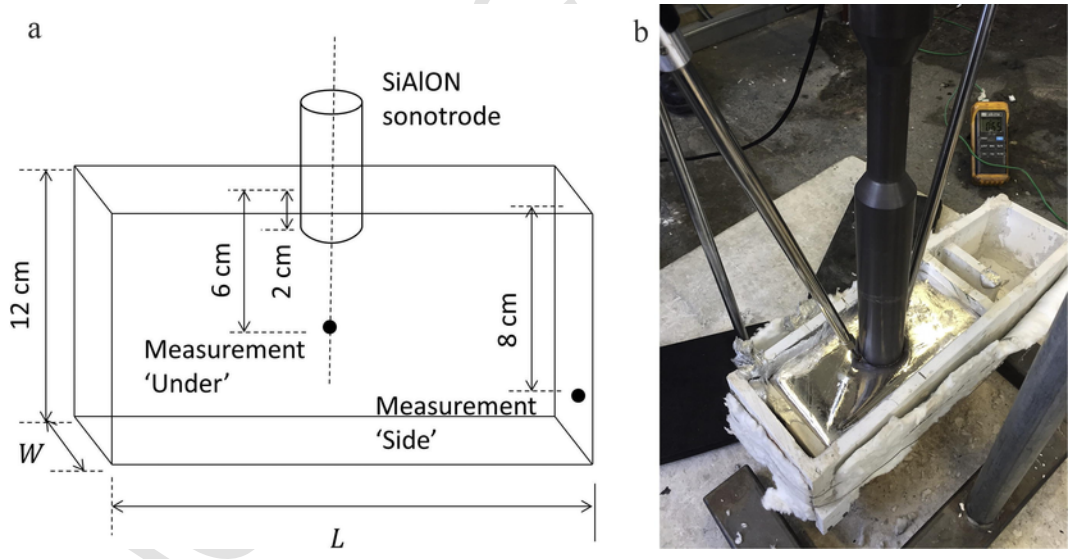

Fig. 1. (a) Schematic of sonication experiment. (b) Liquid aluminium experiment with cavitometers measuring pressures under the sonotrode.

Table 1
Acoustic power delivered to the treated liquids as a function of the transducer power and sonotrode amplitude.

			Power delivered to the liquid (W)			
Power (%)	Peak-to-peak amplitude (μm ± 1 μm)	Power in the air (W)	Aluminium	Ethanol	Glycerol	Water
50	24	49	174	94	300	142
60	27.5	59	220	109	331	166
70	33	69	276	152	437	211

the liquid was estimated as follows: the input electric power when the sonotrode operated the reference medium (air) was subtracted from the power measured in the studied liquid, as listed in Table 1. The experiments were performed in four liquids: deionised water, ethanol, glycerol, and liquid aluminium. Aluminium was selected as a material for comparison because it is extensively studied and widely used in metallurgical, automotive, and aerospace industry as an alloy base.

Table 2 lists the vessel dimensions and the wavelength of sound at 19.6 kHz in each liquid. The temperature of water, ethanol, and glycerol was maintained at 23 ± 1 °C. The temperature of aluminium was maintained at 680 ± 10 °C. There was no controlled atmosphere. For the four liquids, the resonance length of the vessel is equal to the wavelength of the sound wave, as shown in Table 2. A non-wavelength length was chosen for water to gauge whether setting one length to differ from the wavelength of sound at the operating frequency has an effect on the pressure field.

A calibrated high-temperature cavitometer [17] with a spatial resolution of 40–50 mm and a bandwidth of up to 10 MHz recorded pressures at two locations: under the sonotrode (6 cm below the free surface) and at one side of the rectangular domain (8 cm below the free surface) shown with black dots in Fig. 1(a). Each pressure measurement, amplified by a calibrated pre-amplifier and captured by a digital oscilloscope (Picoscope series 4424), was averaged from 60 individual readings, each corresponding to the Fast Fourier Transform (FFT) of a 2 ms signal with resolution of 0.150 kHz each. The data was acquired when there was no change in the average value of the minimum voltages and a steady state condition was achieved. The pressure conversion process followed the recommendations from Hurrell and Rajagopal [33]. A full account of the cavitometer design and performance can be found elsewhere [17]. To ensure reproducibility of the results, each measurement was repeated three times.

2.2. Numerical

2.2.1. Governing equations

The equations governing sound propagation in a moving liquid follow the conservation of mass and momentum:

$$\frac{\partial p}{\partial t} + v_j \frac{\partial p}{\partial x_j} + \rho c^2 \frac{\partial v_j}{\partial x_j} = \rho c^2 \frac{\partial \phi}{\partial t} \tag{1}$$

$$\frac{\partial v_i}{\partial t} + v_j \frac{\partial v_i}{\partial x_j} + \frac{1}{\rho}\frac{\partial p}{\partial x_i} = \frac{\partial \tau_{ij}}{\partial x_j} + F_i \tag{2}$$

p is pressure. v_j are velocity components. ρ is liquid density. $c \equiv \sqrt{\partial p/\partial \rho}$ is the speed of sound in the liquid. $\phi = \frac{4}{3}\pi n_0 R^3$ is the bubble phase fraction, where n_0 is the number of bubbles, each of radius R, per unit volume. The acoustic velocity sources due to the vibrating horn are prescribed in the momentum source term F_i. The term $\frac{\partial \tau_{ij}}{\partial x_j}$ accounts for acoustic energy dissipation due to viscosity. To minimize the effect of numerical dispersion, a high-order finite difference discretization method [34], previously developed by the modelling group at Greenwich, is used to cast Eqs. (1) and (2) into linear equations. The discretized equations are solved explicitly.

The Rayleigh-Plesset equation governs the dynamics of spherical bubbles in the presence of the acoustic field:

$$R\ddot{R} + \frac{3}{2}\dot{R} = \frac{p_s}{\rho} \tag{3}$$

$p_s = p_b(t) + p_v - \frac{2\sigma}{R} - \frac{4\mu\dot{R}}{R} - p(t)$. $p_b = p_{g,0}\left(\frac{R_0}{R}\right)^{3\kappa}$ is the pressure inside the bubble walls, with $p_{g,0}$ being the gas pressure at the equilibrium radius R_0. $\kappa = 0.14$ is the polytropic exponent. p_v is the bubble vapour pressure. σ is the surface tension between the liquid and the bubble gas. μ is the dynamic viscosity of the liquid. The dotted accents denote time derivatives. The Rayleigh-Plesset equation is solved using the explicit version of the 4th Merson method that is implemented in the Intel ODE solver library [35].

Eq. (3) assumes that the cavitating bubbles stay spherical: this assumption is valid because deviations from sphericity have an effect of the order of 2% on the resonant frequency of the bubbles [36]. The developed model is intended for use in aluminium, where the large surface tension value with hydrogen bubbles will tend to keep bubbles spherical.

2.2.2. Initial and boundary conditions

The pressure and velocity components are initially zero. The liquid contains n_0 bubbles per unit volume, each with an equilibrium radius R_0. The driving signal is directly prescribed on the ultrasonic horn by specifying the velocity component normal to its surface as $u_n = 2\pi f A \sin(2\pi f t)$, where f is the driving frequency and A is the displacement amplitude (Table 1).

The sonotrode and tank walls are fully reflective to sound; this is implemented using the mirror technique from [34]. A π-radian phase shift occurs upon reflection from the free surface: this is implemented numerically by fixing the pressures in the row of computational cells above the free surface to 0 Pa. The problem is solved in three-dimensions for a run time of 3 ms in a castellated uniform mesh of the geometry that is illustrated in Fig. 1(a). Castellation is required since the discretization method for the wave equations relies on a uniform grid in each coordinate direction.

2.2.3. Material properties

Table 3 lists the material properties that are used in the numerical simulations.

Table 2
Dimensions of the liquid domain and comparison with wavelength at 19.6 kHz.

Liquid	Water (7.5 cm)	Water (6.5 cm)	Ethanol	Glycerol	Aluminium
Speed of sound c ($m\,s^{-1}$)	1482	1482	1100	2000	4600
Wavelength at 19.6 kHz (cm)	7.4	7.4	5.5	10	23
Length L (cm)	7.5	6.5	5.5	10	23
Width W (cm)	20	20	20	20	15
Liquid height (cm)	12	12	12	12	12

Table 3
Material properties [3,18].

Material	Water	Ethanol	Glycerol	Aluminium melt
Temperature (°C)	20	20	20	700
Density ρ ($kg\,m^{-3}$)	1000	785	1260	2375
Dynamic viscosity μ (10^{-3} Pa s)	1.004	1.1	950	1.0
Speed of sound c ($m\,s^{-1}$)	1482	1100	2000	4600
Surface tension ($N\,m^{-1}$)	0.079	0.022	0.064	0.860
Vapour pressure p_v (kPa)	2.2	5.333	0	0

3. Results

3.1. Pressure conversion

The pressure conversion procedure is illustrated with a reading for water (L = 7.5 cm) with amplitude 50% and at the 'Side' location of the cavitometer. Fig. 2 shows the recorded voltage signals $V(t)$ from the cavitometer and its associated Fourier transforms $\mathcal{F}[V(t)]$ in the calibrated range of the cavitometer.

The sensitivity of the calibrated cavitometer is available in discrete steps of 0.5 kHz between 15 kHz and 50 kHz, as shown in Fig. 3(a). However, the acquired data FFT, shown in Fig. 2(b), is available at frequencies that do not exactly match the calibration frequencies, shown in Fig. 3(a). To convert the voltages to pressures, the sensitivity values $M(f)$ are therefore interpolated to match the frequencies at which the calibration points are acquired (shown in Fig. 3(a)). The result of the operation $\frac{\mathcal{F}[V(t)]}{M(f)}$ is shown in Fig. 3(b). The Fourier transform is converted to a one sided spectrum before the division by the sensitivity.

The pressure recordings are obtained by applying Eq. (4) found in [33] to the raw voltage readings. Fig. 4(a) shows the resulting average pressures of the order of 100 kPa. These pressures include contributions from the ultrasonic source, reflection from walls and the free surface, and the activity of all nearby bubble clouds (including signals from any bubbles that are seeded on the rough surface of the cavitometer).

$$p(t) = \mathcal{F}^{-1}\left[\frac{\mathcal{F}[V(t)]}{M(f)}\right] \tag{4}$$

The maximum and root mean square (RMS) pressures as recorded by the cavitometer in water are therefore 714 kPa and 670 kPa, respectively. This is comparable to a rough estimate that is obtained by directly dividing the raw voltage by the average sensitivity (Fig. 4b). The deconvoluted readings (Fig. 4a) are, however, lower because discarding frequencies outside the calibration range is equivalent to filtering the high-frequency components out, resulting in a smaller signal. In the following text, the pressures obtained from this deconvolution procedure are given along with the pressures estimated by dividing the raw voltage with the average cavitometer sensitivity.

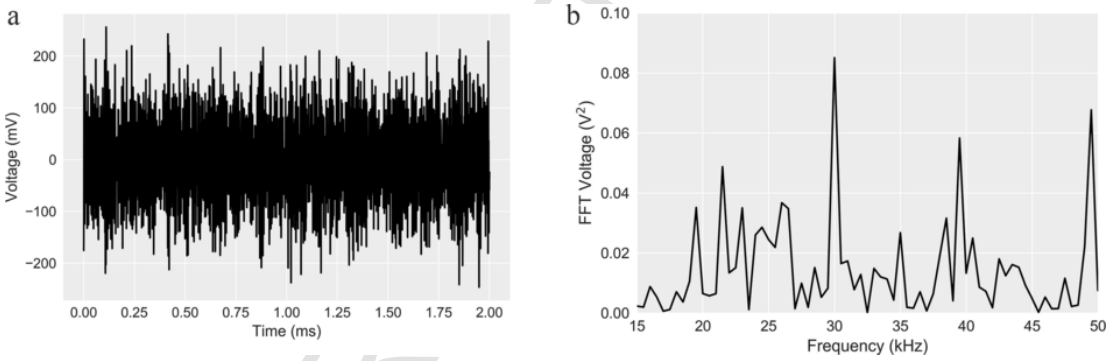

Fig. 2. (a) Raw voltage signals; (b) Fourier transform in the calibration range of the cavitometer.

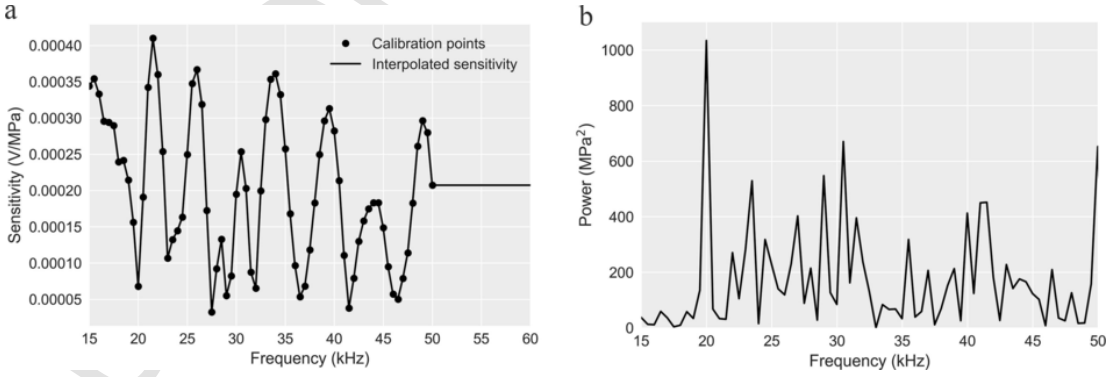

Fig. 3. (a) Sensitivity values for the cavitometer. The markers denote the sensitivity values from a calibration exercise at the National Physical Laboratory [2]. The solid lines are a linear interpolation function passing through the data points. Sensitivity values outside the calibrated range are set to the end values. (b) Results of the division of the Fourier transforms of the voltage signal by the interpolated sensitivity function.

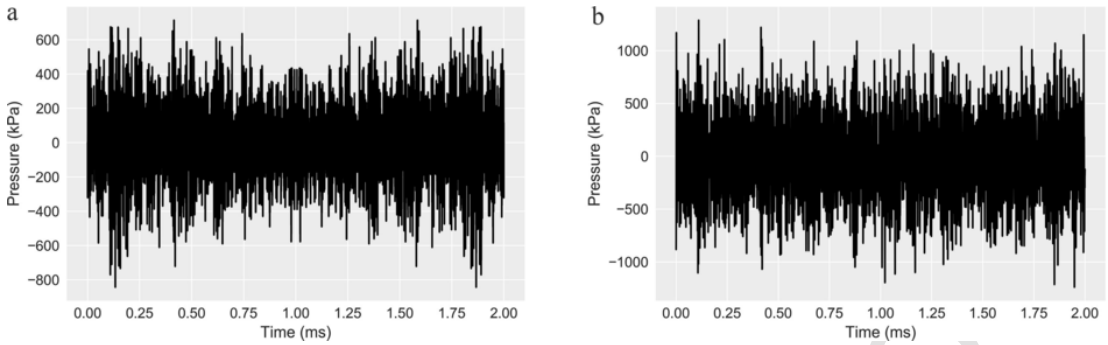

Fig. 4. (a) Pressures obtained using the deconvolution process. (b) Pressures obtained by dividing raw voltage by the average sensitivity = 0.0002 V/MPa.

3.2. Pressure measurements and predictions

Figs. 5 and 6 show the root mean square and maximum pressures measured in each liquid. The numerical prediction is plotted to the right-hand side of the measurements. The numerical pressures (labelled 'Numerical') are extracted from the computational cell whose location is closest to the liquid measuring point. The third column, labelled 'Numerical (Spatial Resolution)', refers to the pressures averaged over the volume covering the spatial resolution of the calibrated cavitometer. The error bars on this column correspond to the range of average pressures obtained with spatial resolutions in the range of 40–50 mm. The error bars in the experimental data points correspond to the bootstrapped confidence interval of all the recordings. 'Experimental Deconvolution' refers to the pressures obtained using the deconvolution procedure outlined in section Pressure Conversion. 'Experimental Average' refers to the pressures obtained by diving raw voltages by the average sensitivity of the calibration process. Both numerical values correspond to the finest mesh used, of cubical computational cells with side length 2 mm.

In water, the pressures (both RMS and maximum) under the sonotrode increase as the amplitude increases. The pressures are larger in the case where $L = 7.5$ cm, which corresponds to the wavelength of sound at the driving frequency. The pressures at the side decrease as

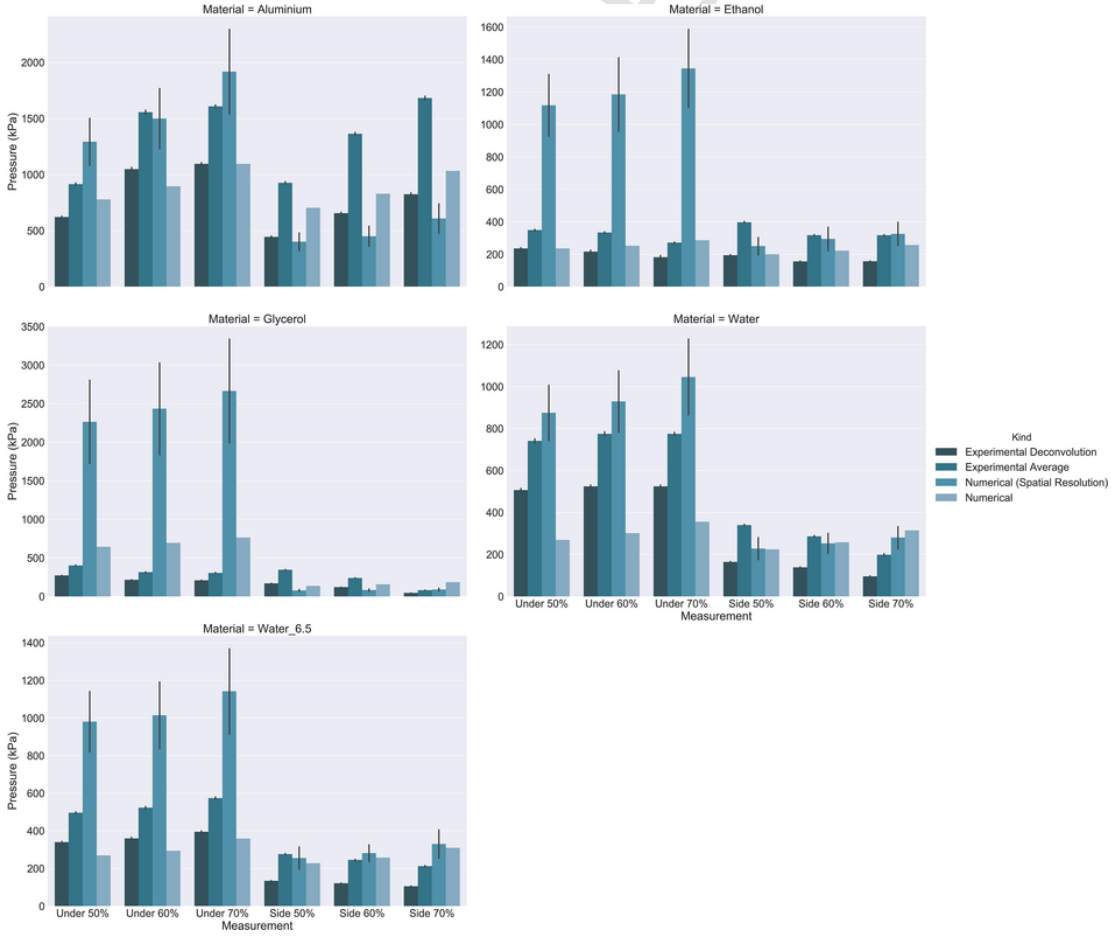

Fig. 5. Variation of the root mean square (RMS) pressures (in kPa) in the tested liquids. Each graph corresponds to measurements and predictions in a particular liquid. 'Water' refers to the water tank with $L = 7.5$ cm, and 'Water_6.5' refers to the corresponding tank with $L = 6.5$ cm. Note the different scales of the Y-axes.

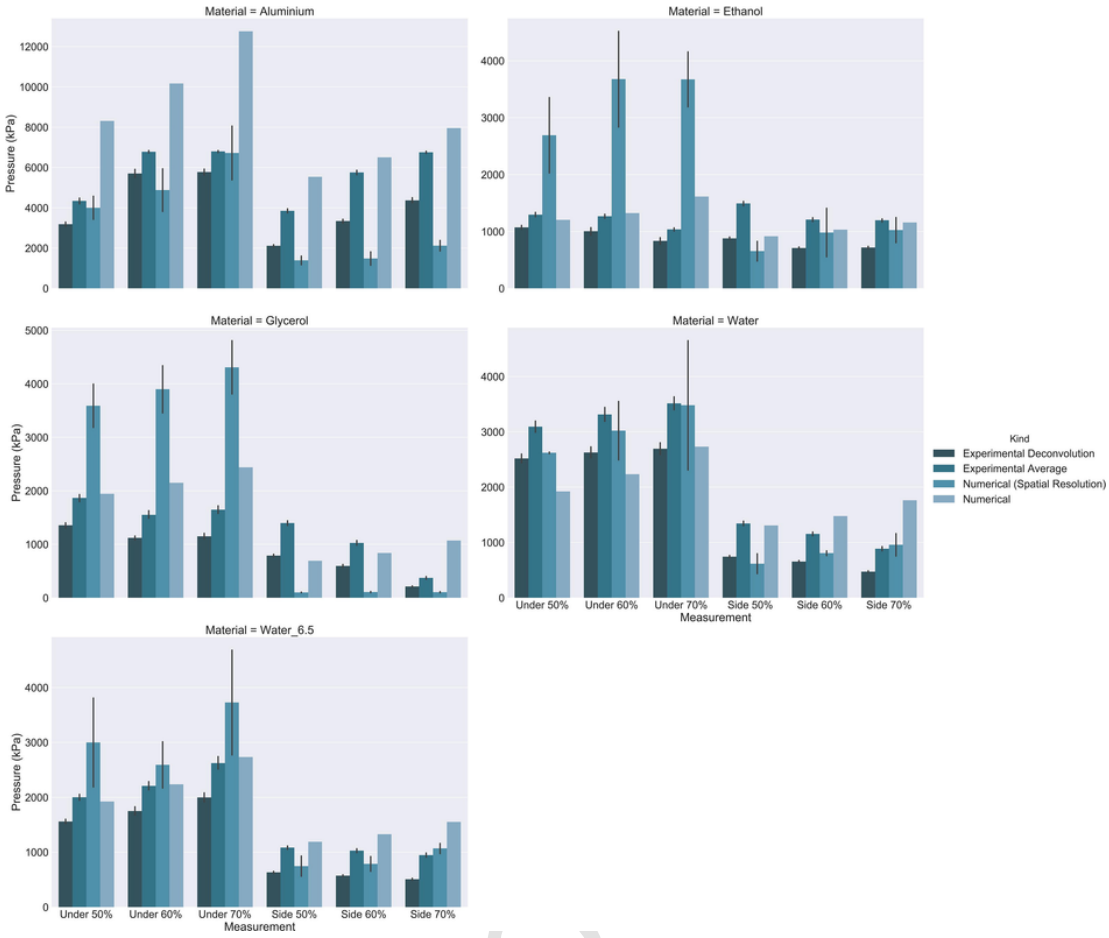

Fig. 6. Maximum pressures recorded in 2 ms intervals for the experimental data. The maximum pressures are recorded in 3 ms of run time for the numerical data. Each graph corresponds to measurements and numerical predictions in a particular liquid. 'Water' refers to the water tank with $L = 7.5$ cm, and 'Water_6.5' refers to the corresponding tank with $L = 6.5$ cm.

amplitude increases. The numerical predictions do not match this behaviour: the numerical results suggest that the pressure is independent of the geometry and does not predict the decrease in pressure with amplitude of the forcing signal. The match between the numerical and experimental pressures is better for the maximum pressures under the sonotrode (Fig. 6) than for the RMS pressures (Fig. 5).

The measured pressures in ethanol and glycerol decrease as the amplitude increases. As in the case for water, the magnitudes of the pressures are over-estimated in modelling, especially the RMS pressures. Specifically, in ethanol a good match is observed between the experimental and numerical predictions for all the cases apart from the 70% acoustic power case, where there is an overestimation of about 30% for the RMS pressure values and about 40% for the maximum pressure. In glycerol, this discrepancy is even higher for measurements under the sonotrode and for acoustic power 70%, though it agrees reasonably well for side measurements at the acoustic power of 50% and 60%. However, the numerically averaged pressures (over the volume corresponding to the spatial resolution of the cavitometer) in both ethanol and glycerol are worse that the numerical pressures extracted under the sonotrode, at the point representing the cavitometer tip in the experiment.

In liquid aluminium, the numerical model overestimation is small for RMS pressures under the sonotrode and slightly larger for RMS pressures on the sides, but the trend of pressure increasing with amplitude is captured correctly. In aluminium, the numerical RMS pressures (Fig. 5) are closer to the experiments than the maximum pressures (Fig. 6). So the model may not predict accurately the trend in variation of the side pressures in water, ethanol, and glycerol but in the case of liquid aluminium, which is the most challenging in this study due the high temperature and opacity, seems to work adequately.

The power spectrum is plotted against the calibration frequency range to infer the frequencies at which the maximum cavitation activity occurs (Figs. 7and 8). The whole spectra comprise the transducer signal superimposed with acoustic resonance from stable periodic oscillating cavitation bubbles. Huang *et al.* [14] suggested that the different magnitudes of bubble radii resulted from the different magnitudes of acoustic intensity applied in liquid. This is in agreement with the findings of this study, as shown in Fig. 8.

For water, ethanol, and glycerol, the maximum power spectrum is at the driving frequency of 19.6 kHz as expected. In aluminium, the highest pressure peak is at around 27 kHz for 60% and 70% input power (Fig. 8). Bubbles in aluminium are unstable at frequencies close to the second harmonic, emitting strong pressure signals prior to their collapse. Minnaert's equation predicts that the bubble linear resonance size in liquid aluminium at ~20 kHz is ~20 μm. The dominant peak is at 27 kHz, which means that bubbles become unstable and at the same time survive for long time period at a slightly lower size. This is more likely the reason, also suggested by Luther *et al.* [37] why significant peaks are not observed in the range of the forcing frequency.

This is also in good agreement with X-ray observations of the statistical size distribution of the cavitation bubbles in liquid aluminium [12,14]. These bubbles survive much longer than just a few excitation cycles in liquid aluminium, in stark contrast to the expected transient

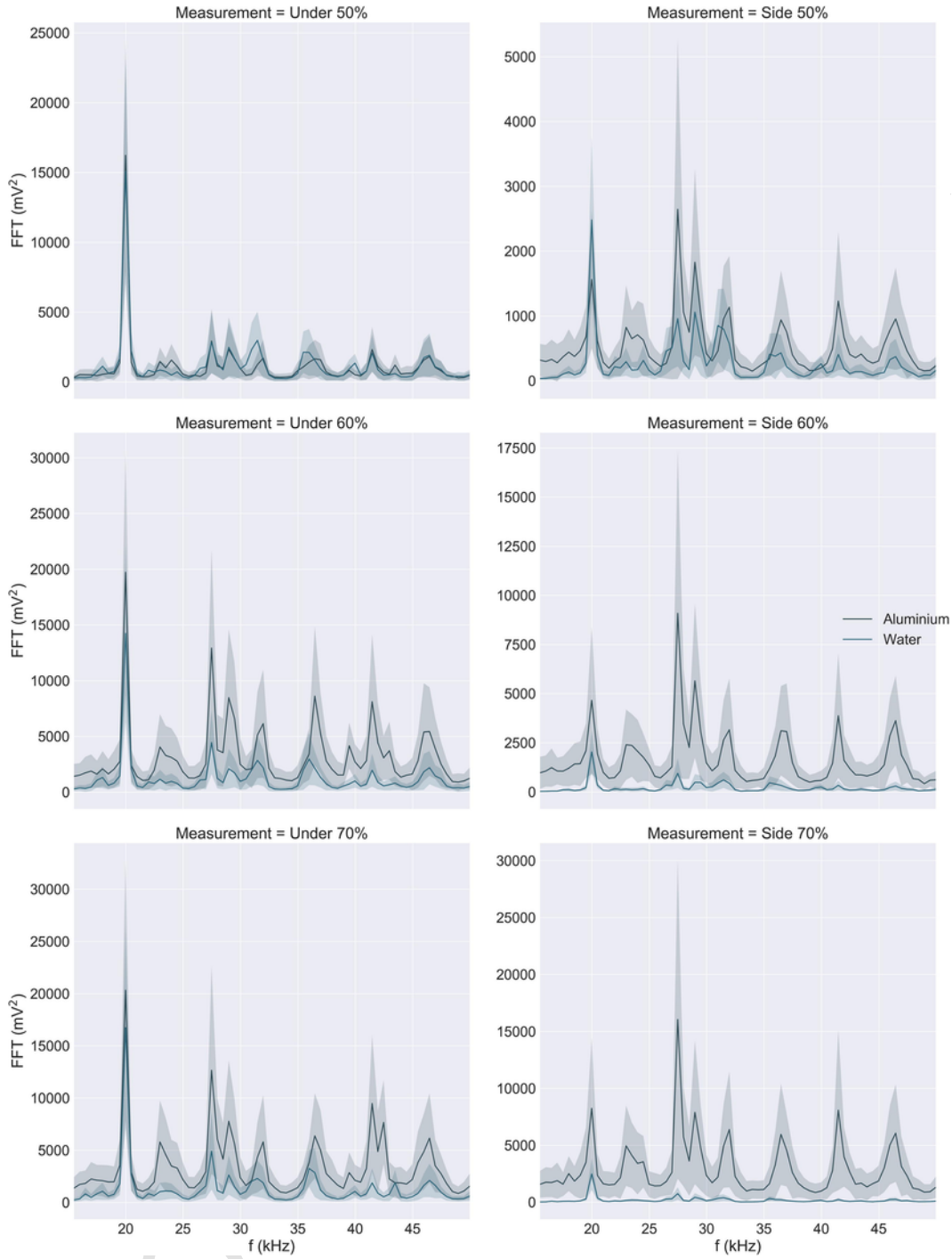

Fig. 7. Power spectra at the two measurements points for aluminium and water at the three power settings. The power spectra are obtained by dividing the raw Fourier transforms by the sensitivities using $\frac{\mathcal{F}[V(t)]}{M(f)}$. The shading corresponds to the bootstrapped 95% confidence interval of the 60 readings.

cavitation behaviour. Again this is in good agreement with the results from [12,14] where the majority of bubbles surviving in similar melts, were in the range of half (or even smaller than) the linear resonance size predicted by the Minnaert equation. Thus, for first time, proper quantification coupling the acoustic pressure field with the size of the cavitation bubbles is achieved within a sonicated liquid metal environment.

3.3. Bubble cloud prediction

Figs. 9 to 12 depict the bubble cloud numerical predictions in the short axis of symmetry of the vessel. These figures represent the contour of the bubble volume fraction ? along the plane of the axis of the horn that is parallel to the length of the tank. For water (Fig. 9), the cloud is independent of the amplitude in the range of 50–70%. This is expected with the acoustic shielding regime already achieved at these

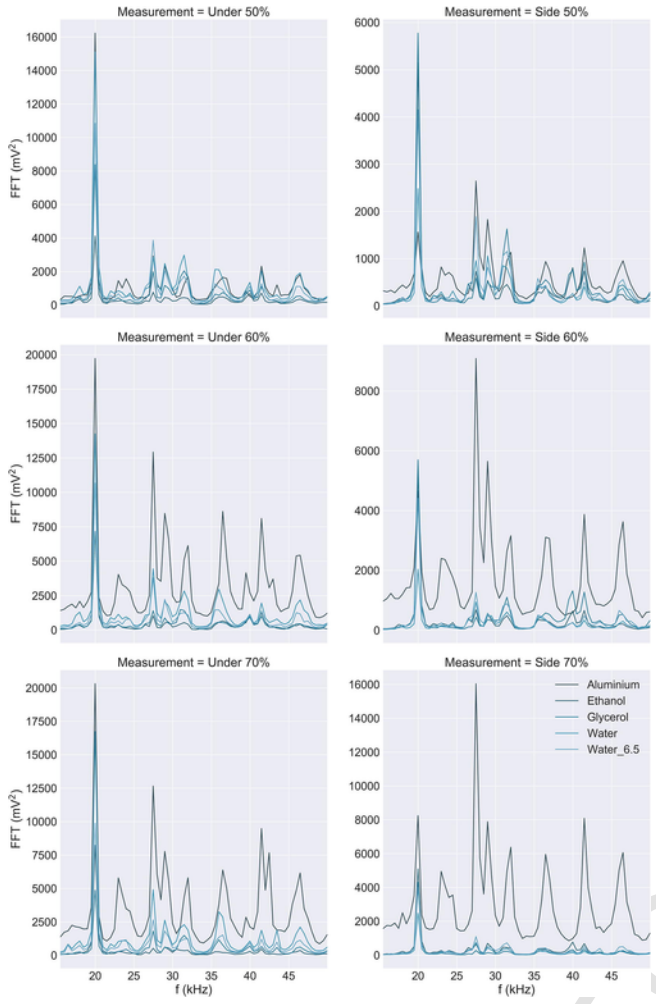

Fig. 8. Mean power spectra for all liquids at the 3 input power settings. The confidence intervals are not plotted for the sake of clarity.

forcing frequencies: hence input power would have no influence on the bubble structures in the liquid.

The bubble spread is more prominent in ethanol (Fig. 10), almost covering the field of view. The high volatility of ethanol encourages the formation of cavitating bubbles throughout the medium, hence leading to cavitation structures everywhere in the liquid. In glycerol (Fig. 11), the bubbles are limited to a small region just below the ultrasonic horn. Due to the large viscosity of glycerol, acoustic pressures are attenuated quickly, confining the active cavitation zone to a small volume below the sonotrode. These numerical predictions agree well with optical observations reported elsewhere [18]. In aluminium (Fig. 12), the bubble cloud length increases with amplitude, with bubble zones present in the middle and edges of the domain at higher amplitudes.

4. Discussion

The effect of the resonance size of the vessel is apparent from the comparison of two water containers with the lengths 7.5 cm (resonance) and 6.5 cm (out of resonance). At 19.7 kHz, resonance is expected with a dimension equal to the wavelength. Larger pressures are therefore expected (Figs. 5–8). Also, the bubble cloud is more elongated (conical shape), confined, and denser at $L = 7.5$ cm as standing waves give rise to the pressure field, alleviating the formation of populated bubbly structures which in turn shield the propagation of acoustic pressure waves from the transducer and the collapsing bubbles (Fig. 9). Thus, if shielding is more pronounced at 7.5 cm, it would normally be expected that the recorded pressures are lower (as every other parameter was kept the same). However, the formation of standing waves which is likely to be more pronounced in the 7.5 cm tank (resonance length) and the super-imposed signal and reflection at the resonant frequency surpass the effect of the geometry/shielding and significantly increase the pressure magnitude. Thus, it is a trade-off between geometry-shielding and geometry-resonance.

The measured pressures suggest that developed acoustic shielding is already present at the amplitudes 50–70% in water, ethanol and glycerol, but not in aluminium. The bubble cloud that is below the horn attenuates the sound propagation: smaller pressure amplitudes are thus measured at the sides. For glycerol, it is presumed that side pressures attenuation is also caused by acoustic dissipation due the large viscosity of the medium. However, the pressures generated by the transducer are not strong enough for the full acoustic shielding regime to be

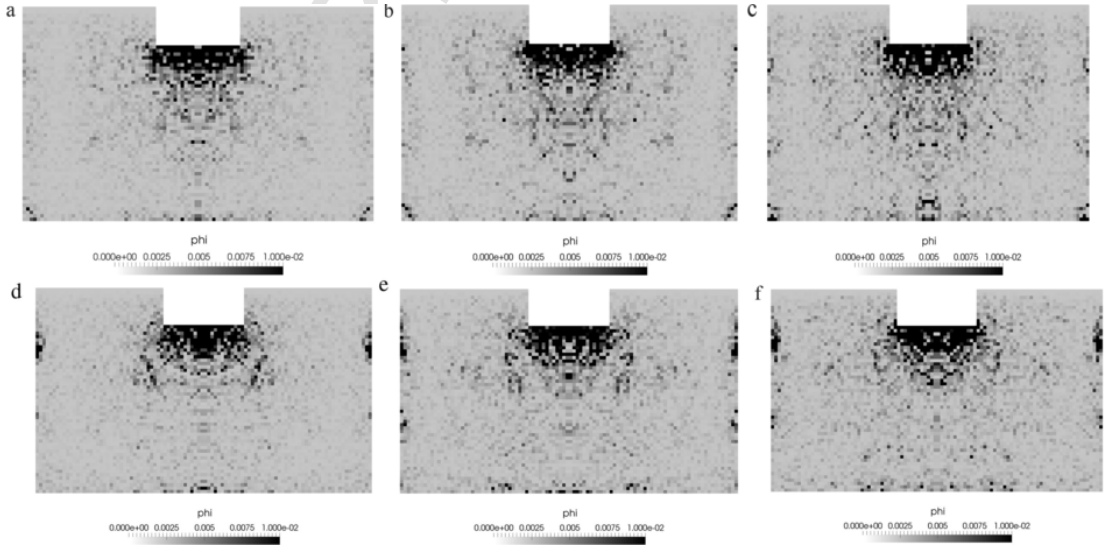

Fig. 9. Numerical simulation of the cavitation zone in water (L = 7.5 cm) (a–c) and water (L = 6.5 cm) (d–f).

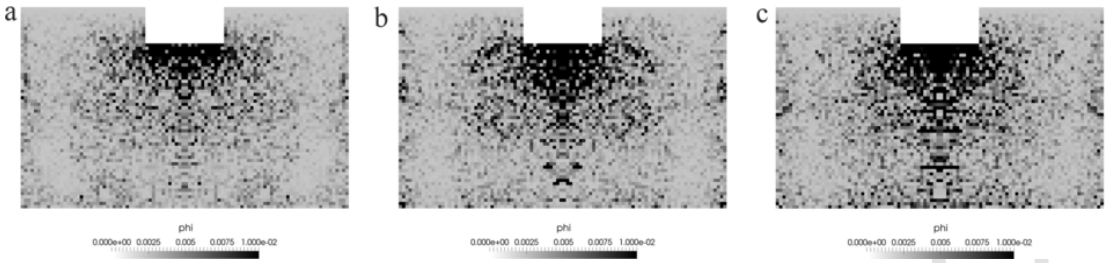

Fig. 10. Numerical simulation of the cavitation zone in ethanol.

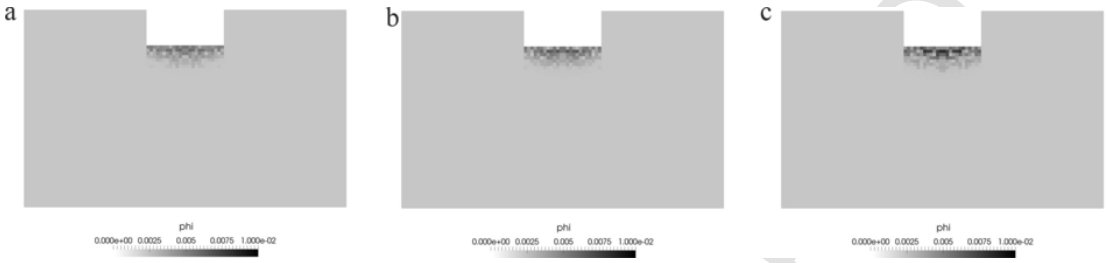

Fig. 11. Numerical simulation of the cavitation zone in glycerol.

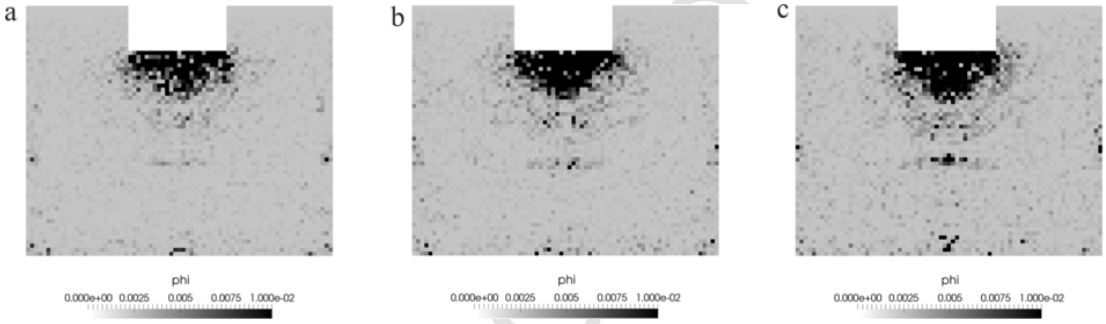

Fig. 12. Numerical simulation of the cavitation zone in liquid aluminium.

reached in liquid aluminium, since the side pressures increase as power increases. This is indirect evidence that there are fewer cavitating bubbles in aluminium at these amplitudes.

Despite qualitatively correct simulation, the inadequate quantitative numerical prediction of acoustic shielding demonstrates that the acoustic cavitation model breaks down at large forcing signals or in the presence of a very viscous medium. An alternative numerical description is required at these amplitudes as the Caflisch model assumes that there is a large separation between bubbles and that the speed of sound is constant throughout the medium, which is not the case at the regime where acoustic shielding occurs. Upon developed cavitation the volume fraction of bubbles is expected to be much higher than the limiting 2% of van Wijngaarden type models, and the bubble density start to affect the speed of sound propagating in the medium [20]. Modelling a cloud as a continuous medium introduces the undesired need to obtain an accurate distribution for the bubble density, another source of modelling error [20]. However, if there are fewer bubbles (as in aluminium), the model is applicable.

The poor prediction of the volume averaged pressures in ethanol and glycerol suggests that the calibration exercise in water is not directly applicable to these two liquids, as they are significantly different to water and aluminium in cavitation and flow behaviour [18]. Since the probe was calibrated in water [17], the correlation between measured pressures and numerical averaged pressures over the volume of the spatial resolution is better for water and aluminium. The good match between the RMS values in aluminium is not surprising since water is the closest physical analogue to aluminium when considering non-dimensional numbers relevant to fluid flow (Re, Oh) [18].

Nevertheless, the qualitative bubble cloud description of the numerical model agrees with the observations of [18]: (i) the conical bubble structure is recovered in water when $L = 7.5$ cm (Fig. 9) and is independent of amplitude after acoustic shielding; (ii) cavitation occurs almost everywhere in the vessel in ethanol (Fig. 10); (iii) cavitation activity is limited below the horn in glycerol (Fig. 11). The main discrepancy lies in the quantitative description of the pressure field.

The difference between RMS pressures in experiments and numerical simulations (Fig. 5) suggests that the acoustic energy is not suitably dissipated in the numerical model when there is acoustic shielding in the three transparent liquids. This is more apparent in glycerol. However, when there is no fully-developed acoustic shielding and the volume fraction of bubbles is still expected to be lower than 1–2%, as in aluminium, the RMS predictions are closer to the measured values. Aluminium behaviour is different from that in the three transparent liquids, both in pressure measurements (larger magnitude) and bubble behaviour.

The experimental setup that is described in the Setup section can record acoustic spectra, using an advanced high temperature cavitometer. This suffices for listening to bubbles emitting sound waves in the calibrated range of the cavitometer (15–50 kHz). The acoustic driving frequency was at 19.7 kHz with the resulting acoustic pressure varying between the different liquids.

Under these conditions, we noticed that in liquid aluminium the maximum peak acoustic pressures were observed at values larger than

the driving frequency of 19.7 kHz. In the other liquids, maximum peak pressures were observed at the driving frequency of 19.7 kHz. This can be explained by the presence of a large number of bubbles with a natural frequency of 27 kHz. Based on this observation, we can assume that majority of bubbles are smaller than the theoretical linear resonance size (~20 μm). This assumption agrees well with the results from [12,14] where the majority of bubbles where indeed tracked in sizes smaller than that of the theoretical linear resonance size.

The dynamic potential of the aluminium cavitation bubbles during ultra-sonication of the melt is highlighted by our results. The power delivered in the melt is significantly lower (~40%, cf Table 1) than that delivered in glycerol. However, the pressure measurements are much higher in aluminium in that particular frequency range and specifically 30–70% higher under the sonotrode and 60–90% (cf Fig. 5) at the side. This emphasizes the effect of shielding and the importance of surface tension, viscosity, and density as dominant factors for regulating the dynamics of bubbles during collapse [1].

In all the liquids, the maximum acoustic pressures as depicted in Fig. 6 are significantly higher than the corresponding RMS values in Fig. 5. Specifically, in the case of water in the 7.5 cm tank, maximum pressures are 6 times higher under the sonotrode and about the same magnitude near the wall. For water in the 6.5 cm tank, the maximum pressure is 5 times higher, both under the sonotrode and at the side corner. For glycerol, pressures were 10 times higher under the sonotrode and 3–4 times larger at the side. For ethanol, maximum pressures were about 4–5 higher than the RMS in the position under the sonotrode and about 4 times in the side. For aluminium, maximum pressures are also 4–6 times larger at both positions. Consequently, as a rule of thumb, maximum cavitation acoustic pressure for all the tested liquids, apart that of glycerol under the sonotrode, exceeds the corresponding RMS pressure about 4–6 times across the whole liquid domain. This generalised observation improves our understanding on the pressure dynamics due to cavitating bubble structures across a fluid domain while at the same time it can be used for further development and validation of numerical models to simulate comprehensively the UST.

In ethanol, (Figs. 5 and 7), measurements are generally insensitive to the position from, or the amplitude of the ultrasonic source. The RMS acoustic pressures were found to be fairly constant and in the range of 150–250 kPa for all the measurement points in liquid ethanol. This is in agreement with our previous observations [1], where we showed that cavitation intensity is similar everywhere in the fluid domain irrespective of the distance and the power input. This is due to the in-phase vibration of numerous cavitation bubbles in the liquid, the multiple reflections from the long lived cavitation bubbles and to the absence of significant bubbly clusters and, hence, shielding.

Water generates a much higher pressure regime compared to that of glycerol due to their different physical properties, especially the higher surface tension and viscosity of glycerol. Water in the tank with resonance length of 7.5 cm seems to have a much higher acoustic pressure under the sonotrode and in the range of about 30% as compared to the 6.5 cm tank, although near the side walls this difference is almost negligible. Interestingly in both tanks, the trend when jumping from a driving power mode to the next one is almost identical, showing a gradual rise of the RMS acoustic pressures. The same occurs for the side walls; however, in this case there is a gradual decay of the pressure signal. Glycerol also follows this trend but at lower scales.

Glycerol has a quite stable performance as the maximum pressure is in similar levels with RMS pressures, in contrast to water where significant increments of maximum pressures are observed. Aluminium and glycerol share some similarities in absolute values of measured acoustic pressures. This is interesting as it shows that the RMS value, which is the main parameter to take into account for evaluation and validation of numerical models, is fairly accurate and closely related to the maximum pressure. This is valid only within the cavitation zone and is in agreement with our recently developed model where it predicts this behaviour [25].

In aluminium, acoustic pressure increases with input acoustic power. Acoustic pressures in liquid aluminium reach the largest values indicating, and especially after the fact that maximum pressure peak is shown at 27 kHz, that cavitation bubbles have a dominant role in the melt, regulating the pressure regime. Measured acoustic pressures in liquid aluminium are in the range of 800–1100 kPa under the sonotrode and in the range of 400–800 kPa in the side.

Comparison between the different length scales of the water tank showed that cavitation development is affected by the vessel size and the resonance mode, giving rise to higher acoustic pressures under resonance conditions. This result reveals that the optimum geometrical features of an experimental tank are located in the range of the resonance size where it is likely that standing waves will be more pronounced.

The maximum acoustic pressures, Fig. 6, which are the instance of a single event among all captured waveforms, showed once again a fairly stable cavitation regime with pressures up to 1.2 MPa in ethanol; higher acoustic pressure peaks in the range of 3 MPa in water with resonance length of 7.5 compare to that with length of 6.5 where pressures were in the range of 2 MPa; glycerol has a very similar performance to that of water in a 6.5 cm tank with pressures reaching up to 1.7 MPa; aluminium achieves the maximum pressures among all the liquids tested, reaching absolute values up to 14 MPa. These are peak incidents, lasting for a very short time of 1–2 μs and, therefore, are not reflected in the predicted RMS pressures of Fig. 5. However, these peaks are presumed to be responsible for deagglomeration of particle clusters and breaking intermetallics present in the liquid pool, thereby enhancing the structure refining process. This is in a very good agreement with the recent experimental work of Wang *et al.* [15] where mechanical breakdown of primary Al_2Cu intermetallic dendrites inside a liquid melt treated using ultrasound achieved by acoustic pressures in the range of 20 MPa. Accordingly the pressures at the side of the vessel followed similar trends but with of course lower absolute values.

5. Conclusions

A numerical model predicts the pressure field in a liquid metal volume across the entire fluid domain, thereby providing a useful tool for optimizing UST. This is of importance as UST can be better controlled and efficiently used, facilitating implementation of this type of processing at the industrial scale.

The effect of acoustic shielding is prominent in resonant vessels. Yet, at the power levels used in this research, acoustic shielding is still not fully achieved in aluminium, providing scope for further optimization of UST of melts. Numerical modelling with the Caflisch equations is inadequate when acoustic shielding is reached. However, a qualitative description of cavitation activity is obtained, with reasonable bubble structures predicted by the model.

Experimental quantification of the acoustic domain within a sonicated liquid metal environment was elucidated for the first time by coupling the acoustic pressure field of this study with the size of the cavitation bubbles previously reported in the literature. This is then supported by our numerical models.

In liquid aluminium, the bubble equilibrium sizes for the three studied powers are smaller than the theoretical linear resonance size giving rise to prominent pressure peaks at frequencies larger than the driving frequency. Furthermore, lifetime effects of the bubbles broaden the spectrum.

Maximum predicted pressures of the order of 10 MPa in liquid aluminium are presumed to be responsible for experimentally observed deagglomeration of particle clusters and breaking of intermetallics present in the liquid pool, thereby enhancing the structure refining process.

The size of the experimental tank plays an important role in the cavitation development as it can significantly increase the acoustic pressure field as demonstrated for the water tank. This contributed to the trade-off between acoustic shielding and acoustic resonance both affected by the geometrical features of the experimental tank.

As a rule of thumb, maximum cavitation acoustic pressure for all the tested liquids, apart that of glycerol under the sonotrode, exceeds the corresponding RMS pressure by about 4–6 times across the entire liquid domain. This generalised observation improves our understanding on the pressure dynamics due to cavitating bubble structures across a fluid domain while at the same time it can be used for further development and validation of numerical models to simulate comprehensively the UST

Future work should focus on the development of an adequately unified model applicable to a variety of liquids with different physical properties; the current model works well and accurately predicts pressure trends in liquid aluminium melts, which was the main point of interest in this research.

Acknowledgement

Financial support from EPSRC (UK) under projects Future Liquid Metal Engineering Hub (EP/N007638/1), UltraMelt (EP/K00588X/1 and EP/K005804/1) and Ultraelt2 (EP/R011001/1, EP/R011044/1 and EP/R011095/1) is gratefully acknowledged. The underlying raw data for the numerical simulations is not shared online due to its size and can be available on request (5.9 TB).

References

[1] O.V. Abramov, Action of high intensity ultrasound on solidifying metal, Ultrasonics 25 (1987) 73–82, https://doi.org/10.1016/0041-624X(87)90063-1.
[2] J. Campbell, Effects of vibration during solidification, Int. Met. Rev. 26 (1981) 71–108, https://doi.org/10.1179/imtr.1981.26.1.71.
[3] G.I. Eskin, D.G. Eskin, Ultrasonic Treatment of Light Alloy Melts, second ed., Taylor & Francis, CRC Press, Boca Raton, 2015.
[4] I. Tzanakis, D.G. Eskin, A. Georgoulas, D.K. Fytanidis, Incubation pit analysis and calculation of the hydrodynamic impact pressure from the implosion of an acoustic cavitation bubble, Ultrason. Sonochem. 21 (2014) 866–878, https://doi.org/10.1016/j.ultsonch.2013.10.003.
[5] F. Wang, D. Eskin, J. Mi, T. Connolley, J. Lindsay, M. Mounib, A refining mechanism of primary Al 3 Ti intermetallic particles by ultrasonic treatment in the liquid state, Acta Mater. 116 (2016) 354–363, https://doi.org/10.1016/j.actamat.2016.06.056.
[6] I. Tzanakis, W.W. Xu, D.G. Eskin, P.D. Lee, N. Kotsovinos, In situ observation and analysis of ultrasonic capillary effect in molten aluminium, Ultrason. Sonochem. 27 (2015) 72–80, https://doi.org/10.1016/j.ultsonch.2015.04.029.
[7] F. Wang, D. Eskin, T. Connolley, J. Mi, Effect of ultrasonic melt treatment on the refinement of primary Al3Ti intermetallic in an Al–0.4Ti alloy, J. Cryst. Growth. 435 (2016) 24–30, https://doi.org/10.1016/j.jcrysgro.2015.11.034.
[8] A. Manoylov, B. Lebon, G. Djambazov, K. Pericleous, Coupling of acoustic cavitation with dem-based particle solvers for modeling de-agglomeration of particle clusters in liquid metals, Metall. Mater. Trans. A 48 (2017) 5616–5627, https://doi.org/10.1007/s11661-017-4321-5.
[9] F. Wang, I. Tzanakis, D. Eskin, J. Mi, T. Connolley, In situ observation of ultrasonic cavitation-induced fragmentation of the primary crystals formed in Al alloys, Ultrason. Sonochem. 39 (2017) 66–76, https://doi.org/10.1016/j.ultsonch.2017.03.057.
[10] D.G. Eskin, K. Al-Helal, I. Tzanakis, Application of a plate sonotrode to ultrasonic degassing of aluminum melt: acoustic measurements and feasibility study, J. Mater. Process. Technol. 222 (2015) 148–154, https://doi.org/10.1016/j.jmatprotec.2015.03.006.
[11] T.V. Atamanenko, D.G. Eskin, L. Zhang, L. Katgerman, Criteria of grain refinement induced by ultrasonic melt treatment of aluminum alloys containing Zr and Ti, Metall. Mater. Trans. A 41 (2010) 2056–2066, https://doi.org/10.1007/s11661-010-0232-4.
[12] W.W. Xu, I. Tzanakis, P. Srirangam, W.U. Mirihanage, D.G. Eskin, A.J. Bodey, P.D. Lee, Synchrotron quantification of ultrasound cavitation and bubble dynamics in Al–10Cu melts, Ultrason. Sonochem. 31 (2016) 355–361, https://doi.org/10.1016/j.ultsonch.2016.01.017.
[13] C. Ruirun, Z. Deshuang, M. Tengfei, D. Hongsheng, S. Yanqing, G. Jingjie, F. Hengzhi, Effects of ultrasonic vibration on the microstructure and mechanical properties of high alloying TiAl, Sci. Rep. 7 (2017) 41463, https://doi.org/10.1038/srep41463.
[14] H. Huang, D. Shu, J. Zeng, F. Bian, Y. Fu, J. Wang, B. Sun, In situ small angle X-ray scattering investigation of ultrasound induced nucleation in a metallic alloy melt, Scr. Mater. 106 (2015) 21–25, https://doi.org/10.1016/j.scriptamat.2015.04.011.
[15] F. Wang, D. Eskin, J. Mi, C. Wang, B. Koe, A. King, C. Reinhard, T. Connolley, A synchrotron X-radiography study of the fragmentation and refinement of primary intermetallic particles in an Al-35 Cu alloy induced by ultrasonic melt processing, Acta Mater. 141 (2017) 142–153, https://doi.org/10.1016/j.actamat.2017.09.010.
[16] G.S.B. Lebon, K. Pericleous, I. Tzanakis, D.G. Eskin, Dynamics of two interacting hydrogen bubbles in liquid aluminum under the influence of a strong acoustic field, Phys. Rev. E 92 (2015) https://doi.org/10.1103/PhysRevE.92.043004.
[17] I. Tzanakis, M. Hodnett, G.S.B. Lebon, N. Dezhkunov, D.G. Eskin, Calibration and performance assessment of an innovative high-temperature cavitometer, Sens. Actuators Phys. 240 (2016) 57–69, https://doi.org/10.1016/j.sna.2016.01.024.
[18] I. Tzanakis, G.S.B. Lebon, D.G. Eskin, K.A. Pericleous, Characterizing the cavitation development and acoustic spectrum in various liquids, Ultrason. Sonochem. 34 (2017) 651–662, https://doi.org/10.1016/j.ultsonch.2016.06.034.
[19] I. Tzanakis, G.S.B. Lebon, D.G. Eskin, K.A. Pericleous, Characterisation of the ultrasonic acoustic spectrum and pressure field in aluminium melt with an advanced cavitometer, J. Mater. Process. Technol. 229 (2016) 582–586, https://doi.org/10.1016/j.jmatprotec.2015.10.009.
[20] I. Tudela, V. Sáez, M.D. Esclapez, M.I. Díez-García, P. Bonete, J. González-García, Simulation of the spatial distribution of the acoustic pressure in sonochemical reactors with numerical methods: a review, Ultrason. Sonochem. 21 (2014) 909–919, https://doi.org/10.1016/j.ultsonch.2013.11.012.
[21] L.V. Wijngaarden, On the equations of motion for mixtures of liquid and gas bubbles, J. Fluid Mech. 33 (1968) 465, https://doi.org/10.1017/S002211206800145X.
[22] R.E. Caflisch, M.J. Miksis, G.C. Papanicolaou, L. Ting, Effective equations for wave propagation in bubbly liquids, J. Fluid Mech. 153 (1985) 259, https://doi.org/10.1017/S0022112085001252.
[23] C. Vanhille, C. Campos-Pozuelo, Nonlinear ultrasonic propagation in Bubbly liquids: a numerical model, Ultrasound Med. Biol. 34 (2008) 792–808, https://doi.org/10.1016/j.ultrasmedbio.2007.11.004.
[24] O. Louisnard, A simple model of ultrasound propagation in a cavitating liquid. Part I: theory, nonlinear attenuation and traveling wave generation, Ultrason. Sonochem. 19 (2012) 56–65, https://doi.org/10.1016/j.ultsonch.2011.06.007.
[25] G.S.B. Lebon, I. Tzanakis, G. Djambazov, K. Pericleous, D.G. Eskin, Numerical modelling of ultrasonic waves in a bubbly Newtonian liquid using a high-order acoustic cavitation model, Ultrason. Sonochem. 37 (2017) 660–668, https://doi.org/10.1016/j.ultsonch.2017.02.031.
[26] D. Fuster, T. Colonius, Modelling bubble clusters in compressible liquids, J. Fluid Mech. 688 (2011) 352–389, https://doi.org/10.1017/jfm.2011.380.
[27] A. Žnidarčič, R. Mettin, M. Dular, Modeling cavitation in a rapidly changing pressure field – Application to a small ultrasonic horn, Ultrason. Sonochem. 22 (2015) 482–492, https://doi.org/10.1016/j.ultsonch.2014.05.011.
[28] L. Nastac, Mathematical modeling of the solidification structure evolution in the presence of ultrasonic stirring, Metall. Mater. Trans. B. 42 (2011) 1297–1305, https://doi.org/10.1007/s11663-011-9539-9.
[29] K. Yasui, Y. Iida, T. Tuziuti, T. Kozuka, A. Towata, Strongly interacting bubbles under an ultrasonic horn, Phys. Rev. E 77 (2008) https://doi.org/10.1103/PhysRevE.77.016609.
[30] K. Yasui, T. Tuziuti, J. Lee, T. Kozuka, A. Towata, Y. Iida, Numerical simulations of acoustic cavitation noise with the temporal fluctuation in the number of bubbles, Ultrason. Sonochem. 17 (2010) 460–472, https://doi.org/10.1016/j.ultsonch.2009.08.014.
[31] K.W. Commander, A. Prosperetti, Linear pressure waves in bubbly liquids: comparison between theory and experiments, J. Acoust. Soc. Am. 85 (1989) 732–746, https://doi.org/10.1121/1.397599.
[32] I. Tzanakis, G.S.B. Lebon, D.G. Eskin, K. Pericleous, Investigation of the factors influencing cavitation intensity during the ultrasonic treatment of molten aluminium, Mater. Des. 90 (2016) 979–983, https://doi.org/10.1016/j.matdes.2015.11.010.
[33] A.M. Hurrell, S. Rajagopal, The Practicalities of Obtaining and Using Hydrophone Calibration Data to Derive Pressure Waveforms, IEEE Trans. Ultrason. Ferroelectr. Freq. Control. 64 (2017) 126–140, https://doi.org/10.1109/TUFFC.2016.2594770.
[34] G.S. Djambazov, C.-H. Lai, K.A. Pericleous, Staggered-mesh computation for aerodynamic sound, AIAA J. 38 (2000) 16–21, https://doi.org/10.2514/2.948.
[35] Y. Laevsky, Intel® Ordinary Differential Equation Solver Library, Intel Corporation, 2008.
[36] M. Strasberg, The Pulsation Frequency of Nonspherical Gas Bubbles in Liquids, J. Acoust. Soc. Am. 25 (1953) 536–537, https://doi.org/10.1121/1.1907076.
[37] S. Luther, R. Mettin, P. Koch, W. Lauterborn, Observation of acoustic cavitation bubbles at 2250 frames per second, Ultrason. Sonochem. 8 (2001) 159–162, https://doi.org/10.1016/S1350-4177(01)00073-6.